

## MAGNETIC TITANIUM-PILLARED CLAYS (Ti-M-PILC): MAGNETIC STUDIES AND MÖSSBAUER SPECTROSCOPY

CHERIFA BACHIR<sup>1,2,\*</sup>, YANHUA LAN<sup>3</sup>, VALERIU MEREACRE<sup>3</sup>, ANNIE K. POWELL<sup>3</sup>, CHRISTIAN BENDER KOCH<sup>4</sup>,  
AND PETER G. WEIDLER<sup>1,\*</sup>

<sup>1</sup> Institute of Functional Interfaces, Forschungszentrum Karlsruhe, Hermann-von-Helmholtz-Platz 1,  
D-76344 Eggenstein-Leopoldshafen, Germany

<sup>2</sup> Department of Industrial Chemistry, Faculty of Sciences, B.P. 1505 EL-Mnaouer, University of Sciences and Technologies  
USTO ‘Mohamed Boudiaf’, Oran, Algeria

<sup>3</sup> Institute for Inorganic Chemistry, University of Karlsruhe (TH), Engesserstr. 15 Geb. 30.45, D-76131 Karlsruhe, Germany

<sup>4</sup> Department of Basic Sciences and Environment, Faculty of Life Sciences, University of Copenhagen, Thorvaldsensvej 40,  
DK-1871 Frederiksberg, Denmark

**Abstract**—Pillared clays (PILCs) with magnetic properties are materials with potential for wide application in industry and the environment, but only a few studies of these types of materials have been carried out. The purpose of this study was to advance knowledge of the preparation and magnetic properties of pillared clays by examining in detail a series of magnetic Ti-pillared clays (Ti-M-PILCs). Samples were synthesized at ambient temperature by sodium borohydride reduction of ferrous ions added by ion-exchange to Ti-pillared montmorillonite (Ti-PILCs). The properties of the Ti-M-PILCs were investigated using a superconducting quantum interference device (SQUID) and Mössbauer spectroscopy. Hysteresis, zero-field-cooled (ZFC), and field-cooled (FC) regimes were measured on different precursor materials prepared by calcination of Ti-PILCs at temperatures between 200 and 600°C. Hysteresis loops, recorded between –7 and 7 T in the temperature range 200–300 K, were observed in most samples depending on the preparation of clays. The ZFC/FC measurements were made after heating from 2 to 300 K under an applied magnetic field of 39.8 kA m<sup>-1</sup>. The influence of the calcination temperature of the starting Ti-PILCs on the structural and magnetic properties of the Ti-M-PILCs was examined. The presence of two different Fe-alloy distributions was found; a dispersed one for the less-calcined Ti-PILCs and clusters for the more-calcined ones.

**Key Words**—Magnetic Properties, Montmorillonite, Mössbauer Spectroscopy, Titanium Magnetic Pillared Clays, ZFC/FC.

### INTRODUCTION

New and innovative methods are required when devising technologies for dealing with environmental problems. The application of magnetic-particle technology to solve environmental problems has received considerable attention in recent years. Magnetic particles can be used to adsorb contaminants from aqueous effluents, with the adsorbent separated from the medium by a simple magnetic process after the adsorption. An example of this technology is the use of magnetite particles to accelerate the coagulation of sewage (Booker *et al.*, 1991).

The combination of interesting adsorption properties of materials with their magnetic properties to produce novel adsorbents is of much interest, *e.g.* the use of magnetic nanoparticles consisting of polyacrylic acid-bound Fe oxide in the adsorption of methylene blue (Mak and Chen, 2004). Another example is the use of

activated carbon/Fe oxide magnetic composites in the adsorption of volatile organic compounds (Oliveira *et al.*, 2002) and the use of montmorillonite-Fe oxide magnetic composites in the adsorption of metal cations (Oliveira *et al.*, 2003).

Clays are cheap and readily available and are excellent cation exchangers; they are used widely in adsorption and catalysis. One important class of clay derivatives is pillared clays obtained from the insertion of metal oxide species into the clay (Kloprogge, 1998). Pillared clays with magnetic behavior would be effective magnetic carriers suitable in a wide range of applications, such as magnetic separation. In the first synthesis of magnetic montmorillonite, NaBH<sub>4</sub> solution was used as a reducing agent for an Fe-exchanged montmorillonite (Zhang and Manthiram, 1996). Similar techniques have also been applied in pillared montmorillonite matrices (Naguib *et al.*, 2003) with slight modifications. In the present work, new, magnetically layered Ti-M-PILCs were prepared and characterized. Magnetic characterizations based on the SQUID magnetometer were carried out in conjunction with Mössbauer spectroscopy and included hysteresis and ZFC/FC measurements to give a detailed view of the behavior of the materials in question.

\* E-mail addresses of corresponding authors:  
Cherifa.Bachir@ifg.fzk.de, bachir\_c04@yahoo.fr,  
peter.weidler@ifg.fzk.de  
DOI: 10.1346/CCMN.2009.0570404

## MATERIALS AND METHODS

The starting clay was montmorillonite SWy-2, from Wyoming, USA, supplied by The Clay Minerals Society Source Clays Repository (Purdue University, Lafayette, Indiana, USA). The montmorillonite was purified by a conventional sedimentation method, collecting the  $<2\text{ }\mu\text{m}$  fraction, and exchanged with NaCl solution to obtain Na-montmorillonite (Na-SWy-2). The homoionic material has a specific surface area (SSA) of  $50\text{ m}^2/\text{g}$ ; a basal spacing,  $d_{001}$ , of  $1.24\text{ nm}$ ; a cation exchange capacity (CEC) of  $85\text{ meq}/100\text{ g}$ ; and the following chemical composition (reported as wt.% oxides): SiO<sub>2</sub> 60.42; Al<sub>2</sub>O<sub>3</sub> 19.79; Fe<sub>2</sub>O<sub>3</sub> 3.99; MgO 2.34; CaO 0.13; Na<sub>2</sub>O 2.21; K<sub>2</sub>O 0.11; TiO<sub>2</sub> 0.11.

### *Preparation of Ti-PILC*

The Ti-PILCs were prepared using the method of Sterte (1986). TiCl<sub>4</sub> was hydrolyzed in 6 M HCl and diluted with water to a final concentration of [Ti<sup>4+</sup>] = 0.82 M. This solution was aged for 3 h before mixing with a 0.4 wt.% Na-SWy-2 suspension in a ratio of 10 mmol Ti<sup>4+</sup>/g clay. After 16 h of exchange, the intercalated clay was centrifuged, washed free of chloride, and dried at 60°C. The Ti-PILCs were obtained by calcination of the intercalated material at 200–600°C for 3 h in air.

### *Preparation of Ti-M-PILC*

Magnetic properties were imparted to the Ti-PILCs (Zhang and Manthiram, 1996; Naguib *et al.*, 2003) by ion-exchange of the interlayer Na<sup>+</sup> ion with a solution of excess ferrous Fe (0.2 M FeCl<sub>2</sub>.4H<sub>2</sub>O) and stirring on a magnetic stirrer for 24 h. The products were centrifuged and washed several times until chloride-free and dried at 60°C. 1 g of the Fe-exchanged Ti-PILCs was then suspended in 50 mL of deionized water and stirred. A freshly prepared solution of 0.5 M NaBH<sub>4</sub> was then added slowly to the suspension at room temperature. The product was separated, freeze dried, and stored in a desiccator. The original pillared samples are designated Ti-PILC, followed by the corresponding calcination temperature (Ti-PILC-temperature [in °C]). For the magnetic pillared samples the notation Ti-M-PILC-temperature is used (M for magnetic).

## METHODS

X-ray diffraction (XRD) was carried out using a Siemens D5000 diffractometer equipped with a graphite diffracted-beam monochromator and CuK $\alpha$  radiation ( $\lambda = 1.5418\text{ \AA}$ ) at 40 kV and 40 mA. In order to optimize the (001) intensities of pillared clays, oriented clay-aggregate specimens were prepared by drying clay suspensions onto glass slides. The XRD patterns were recorded over the range 2 to 12°2 $\theta$  (step size 0.02°2 $\theta$ , step time 4 s) for samples on glass slides, and over the range 2 to 72°2 $\theta$

(step size 0.025°2 $\theta$ , step time 10 s) for powder samples. X-ray fluorescence (XRF) measurements were performed using a MagiXPRO spectrometer from Philips, equipped with a rhodium X-ray tube, on air-dried powdered samples fused with lithium tetraborate. Nitrogen adsorption measurements were performed using a Quantachrome Autosorb-1MP instrument in the relative pressure range  $p/p_0$  from  $10^{-5}$  to 1. The samples were outgassed overnight at 110°C prior to the adsorption analysis. The SSA was calculated according to the BET equation (Brunauer *et al.*, 1938). The non-local density functional theory (NLDFT) has been shown to give quantitatively correct pore-size distributions in silica materials with cylindrical mesopores (Neimark and Ravikovich, 2001; Ravikovich and Neimark, 2001), and extended to the range of micropores (Thommes *et al.*, 2006). For Ti-PILCs and Ti-M-PILCs, the NLDFT was used to calculate the total pore volume ( $V_p$  at  $p/p_0 = 0.7$ ), micropore volume ( $V_{mp}$ ), and mesopore volume ( $V_{mes}$ ) from the adsorption branch, assuming cylindrical pore geometry. The CEC was measured by copper-triethylenetetramine exchange according to the method of Meier and Kahr (1999). The concentration of the Cu-triethylenetetramine complex, [Cu(trien)]<sup>2+</sup>, was determined by photometry ( $\lambda = 580\text{ nm}$ ) in the clear supernatant using a UV-Vis Spectrophotometer, Genesys 10 UV. The attenuated total reflectance infrared (FTIR-ATR) spectra were obtained using a Bruker IFS66 with a DTGS detector and globar source. The ATR device was a Golden Gate single-reflection diamond cell and the powder samples were pressed onto the diamond with a torque of 90 cNm. For each sample, 64 scans in the mid-infrared region (400–4000 cm<sup>-1</sup>) were recorded at a resolution of 4 cm<sup>-1</sup>. In order to emphasize differences due to pillaring and the magnetization process, Na-SWy-2 was used as the background. Mössbauer spectra were acquired using a conventional spectrometer in the constant acceleration mode equipped with a <sup>57</sup>Co source (3.7 GBq) in rhodium matrix. Isomer shifts are given relative to the centroid of the spectrum of  $\alpha$ -Fe at room temperature. The sample was inserted in an Oxford Instruments Mössbauer-Spectromag 4000 Cryostat and the sample temperature was varied between 3 and 300 K. The magnetic measurements were carried out using a Quantum Design SQUID magnetometer MPMS-XL, which works between 1.8 and 400 K and dc applied fields ranging from -7 to 7 T. Measurements were performed on a polycrystalline sample placed in a plastic container. The mass of samples used for measurements were between 10 and 13 mg each. Hysteresis curves were recorded between -7 and 7 T at 2, 5, 10, 50, 100, and 300 K. The specific saturation magnetization ( $M_s$ ), saturation remanent magnetization ( $M_{rs}$ ), coercivity ( $H_c$ ), coercivity of remanence ( $H_{cr}$ ), magnetic squareness ( $M_{rs}/M_s$ ), and the  $H_{cr}/H_c$  ratio were determined from the hysteresis curves. The ZFC/FC measurements were carried out as follows: after the sample was cooled

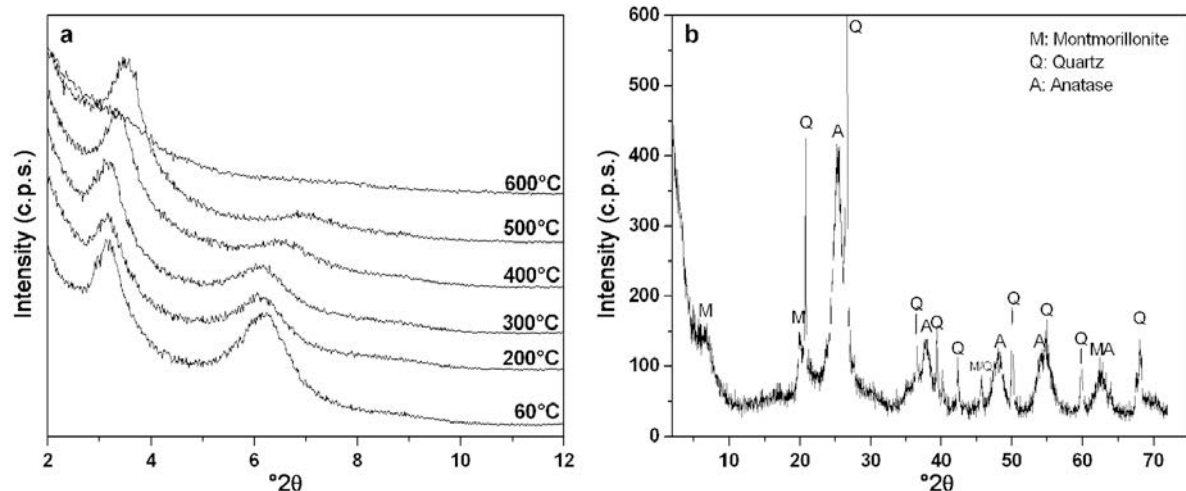


Figure 1. (a) XRD patterns of oriented Ti-pillared clay, dried at 60°C and calcined at various temperatures, and (b) powder XRD pattern of Ti-PILC-600.

from 300 to 2 K at  $H = 0$  kA m $^{-1}$ , a field of 39.8 kA m $^{-1}$  was applied at  $T = 2$  K and the ZFC magnetization  $M_{ZFC}$  (and the corresponding susceptibility  $\chi_{ZFC}$ ) was measured between 2 and 300 K. The sample was again cooled to 2 K in the presence of the same field  $H$  and the temperature dependence of FC magnetization,  $M_{FC}$  ( $\chi_{FC}$ ), was measured between 300 and 2 K. The Weiss constant,  $\theta$ , and Curie constant,  $C$ , were determined by fitting the data of  $\chi_{FC}$  deduced from FC curves at 39.8 kA m $^{-1}$  to the Curie-Weiss law (Morrish, 1965, Suzuki *et al.*, 2003) in the paramagnetic region given by:

$$\chi_{FC} = \text{const} + C/(T - \theta) \quad (1)$$

where  $T$  is the temperature. The fitting procedure was carried out using *CoStat* version 6.303 from Cohort software.

## RESULTS AND DISCUSSION

### Structure and magnetic properties

**XRD.** The pillaring of the clays was characterized by the evolution of the (001) diffraction line and the textural properties. For all samples except Ti-PILC-600, an increase in  $d_{001}$ , due to the insertion of the Ti pillars into the interlayer space, was observed (Figure 1). A constant  $d$  value of 2.80 nm was found for Ti-PILC-60, -200, and -300. At greater temperatures, the  $d$  value decreased with increasing calcination temperature from 2.65 nm for Ti-PILC-400 to 2.50 nm for Ti-PILC-500. A second peak at  $\sim 6^{\circ}2\theta$  decreased in intensity with increasing calcination temperature. The presence of the latter peak was interpreted as the (002) diffraction line of Ti-PILCs. Though the pillaring of the clay structure was not complete after calcination at 600°C, the XRD pattern still showed peaks attributable to montmorillonite, as well as quartz and anatase (Figure 1b).

After insertion of the Fe and subsequent reduction by NaBH<sub>4</sub>, the interlayer spacing decreased to values between 1.6 nm for the samples with smaller calcination temperatures and 1.3 nm for the samples with greater calcination temperatures (Figure 2).

**SSA and porosity.** N<sub>2</sub> adsorption analysis results (Table 1) showed that SSAs were in the range 200–300 m<sup>2</sup>/g and indicated that the pillaring process was successful. On one hand, thermal treatment up to 600°C transformed the polycations into oxide pillars and had no significant impact on the SSA, indicating good thermal stability of the Ti-PILC clay. On the other hand, Ti-PILCs exhibited both micro- and mesoporosity (Table 1). The small CEC values after pillaring suggest the irreversibility of cation exchange; the intercalated Ti polycations were scarcely exchanged. Thus, the CEC

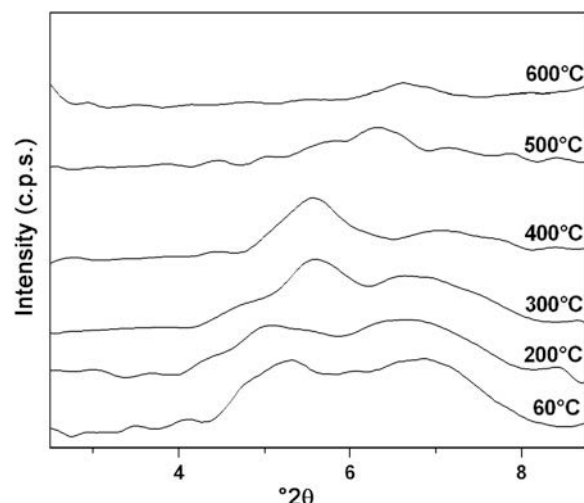


Figure 2. XRD patterns of oriented Ti-M-PILC.

Table 1. Specific surface area, pore volume, and CEC of Ti-PILCs.

Samples	SSA (m <sup>2</sup> /g)	$V_{mp}$ (cm <sup>3</sup> /g)	$V_{mes}$ (cm <sup>3</sup> /g)	$V_p$ (cm <sup>3</sup> /g)	CEC meq/100 g
Ti-PILC-60	281	0.025	0.143	0.169	30
Ti-PILC-200	280	0.017	0.154	0.171	25
Ti-PILC-300	268	0.008	0.161	0.169	23
Ti-PILC-400	262	0.010	0.151	0.160	15
Ti-PILC-500	244	0.005	0.154	0.158	13
Ti-PILC-600	231	0.008	0.145	0.153	12

SSA: specific surface area,  $V_p$ : pore volume at  $p/p_0 = 0.7$  (pore width  $\leq 7$  nm),  $V_{mp}$ : micropore volume,  $V_{mes}$ : mesopore volume, CEC: cation exchange capacity.

value only represented the exchanged residual interlayer cations such as  $\text{Na}^+$ ,  $\text{K}^+$ ,  $\text{Mg}^{2+}$ , and  $\text{Ca}^{2+}$ . After exchange of Fe and  $\text{NaBH}_4$  reduction (magnetization), both the SSA and porosity decreased (Table 2). This decrease was accentuated in the case of Ti-M-PILC-60 and Ti-M-PILC-200. The additional Fe content in Ti-M-PILCs was constant for all samples and did not exceed 2%.

**FTIR-ATR investigation.** Attenuated total reflectance is a rapid, simple, and very useful technique to characterize the surfaces of minerals and was used here to determine whether larger amounts of Fe oxides were present on the outer mineral surfaces. The structural OH-bending mode in montmorillonite absorbed IR radiation between 700 and 950 cm<sup>-1</sup> and exhibited a series of peaks depending on the cations present in the octahedral sheet. In the case of Ti-PILCs, two bands were observed at 913 and 875 cm<sup>-1</sup> for all calcination temperatures (Figure 3a), and these have been assigned to the deformation of Al-Al-OH and Al-Fe-OH groups, respectively (Madejová and Komadel, 2001; Farmer, 1974). The appearance of a weak band at 797 cm<sup>-1</sup> indicated either the presence of traces of poorly crystalline silica (Si-O stretching of quartz and free silica) or Mg-Mg-OH vibrations. The band observed at 975 cm<sup>-1</sup> was related to the stretching of the Si-O group. A slight shift of the latter peak to greater wavenumber (986 cm<sup>-1</sup>) with increasing calcination temperature was observed and was related to the dehydroxylation effect after calcina-

tion. This finding was supported by the decrease in the CEC (Table 1). As indicated by the XRD results of Ti-PILC-600, montmorillonite was still present in the sample. The ATR spectra showed no major differences upon calcination at 600°C. Following the magnetization (Figure 3b), identifying additional bands was not possible, specifically bands indicative of Fe-bearing phases. The results suggested that these phases were not present on the outer surfaces of the Ti-M-PILCs.

**Hysteresis curves (2, 5, 10, 50, 100, and 300 K).** The hysteresis curves of Ti-M-PILC-200 and Ti-M-PILC-300 exhibited a similar shape to that of Ti-M-PILC-60, and those of Ti-M-PILC-400 and Ti-M-PILC-600 were similar to that of Ti-M-PILC-500. Thus, only the shapes of Ti-M-PILC-60 and -500 are presented (Figure 4). For Ti-M-PILC-60, hysteresis obtained at 50, 100, and 300 K had small areas (Figure 4b). At 2, 5, and 10 K almost no hysteresis was obtained. Sample Ti-M-PILC-500 (Figure 4d) revealed a pronounced hysteresis at all measurement temperatures, suggesting ferro(i)magnetic behavior. Saturation magnetization increased further with decreasing temperature for both Ti-M-PILC-60 and Ti-M-PILC-500 (Figure 4). Ti-PILCs are only paramagnetic and so no hysteresis was obtained.

**Temperature dependence of hysteresis parameters.** The variations in the  $M_s$ ,  $M_{rs}$ ,  $H_c$ , and  $M_{rs}/M_s$  of Ti-M-PILCs as a function of the SQUID measurement temperature

Table 2. Specific surface area, pore volume, and amount of additional Fe of Ti-M-PILCs.

Samples	SSA (m <sup>2</sup> /g)	SSA <sub>reduction</sub> * (%)	$V_{mp}$ (cm <sup>3</sup> /g)	$V_{mes}$ (cm <sup>3</sup> /g)	$V_p$ (cm <sup>3</sup> /g)	$V_p$ reduction* (%)	Fe <sub>2</sub> O <sub>3</sub> <sup>add</sup> (wt.%)
Ti-M-PILC-60	65	77	0.003	0.047	0.051	70	1.70
Ti-M-PILC-200	137	51	0.006	0.092	0.099	42	1.83
Ti-M-PILC-300	180	33	0.006	0.118	0.125	26	1.67
Ti-M-PILC-400	211	20	0.007	0.129	0.136	15	1.63
Ti-M-PILC-500	175	28	0.004	0.110	0.114	28	1.60
Ti-M-PILC-600	168	27	0.003	0.111	0.114	26	1.75

Fe<sub>2</sub>O<sub>3</sub><sup>add</sup>: the additional Fe content after magnetization.

\*: Reduction of SSA and  $V_p$  relates to Ti-PILC.

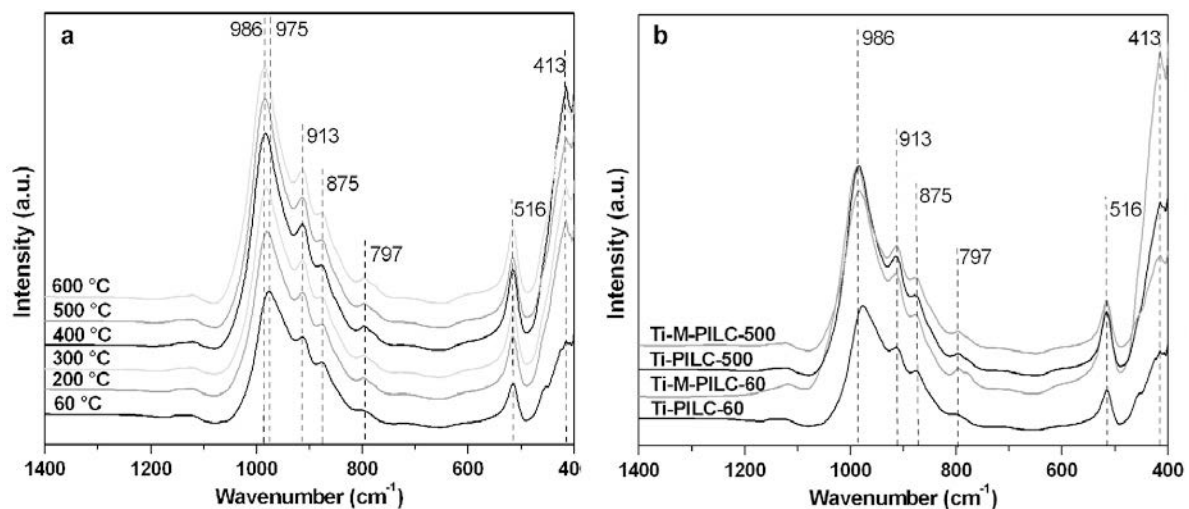


Figure 3. FTIR-ATR spectra of: (a) Ti-PILCs and (b) comparison of Ti-PILC-60 and Ti-PILC-500 with their respective magnetic forms.

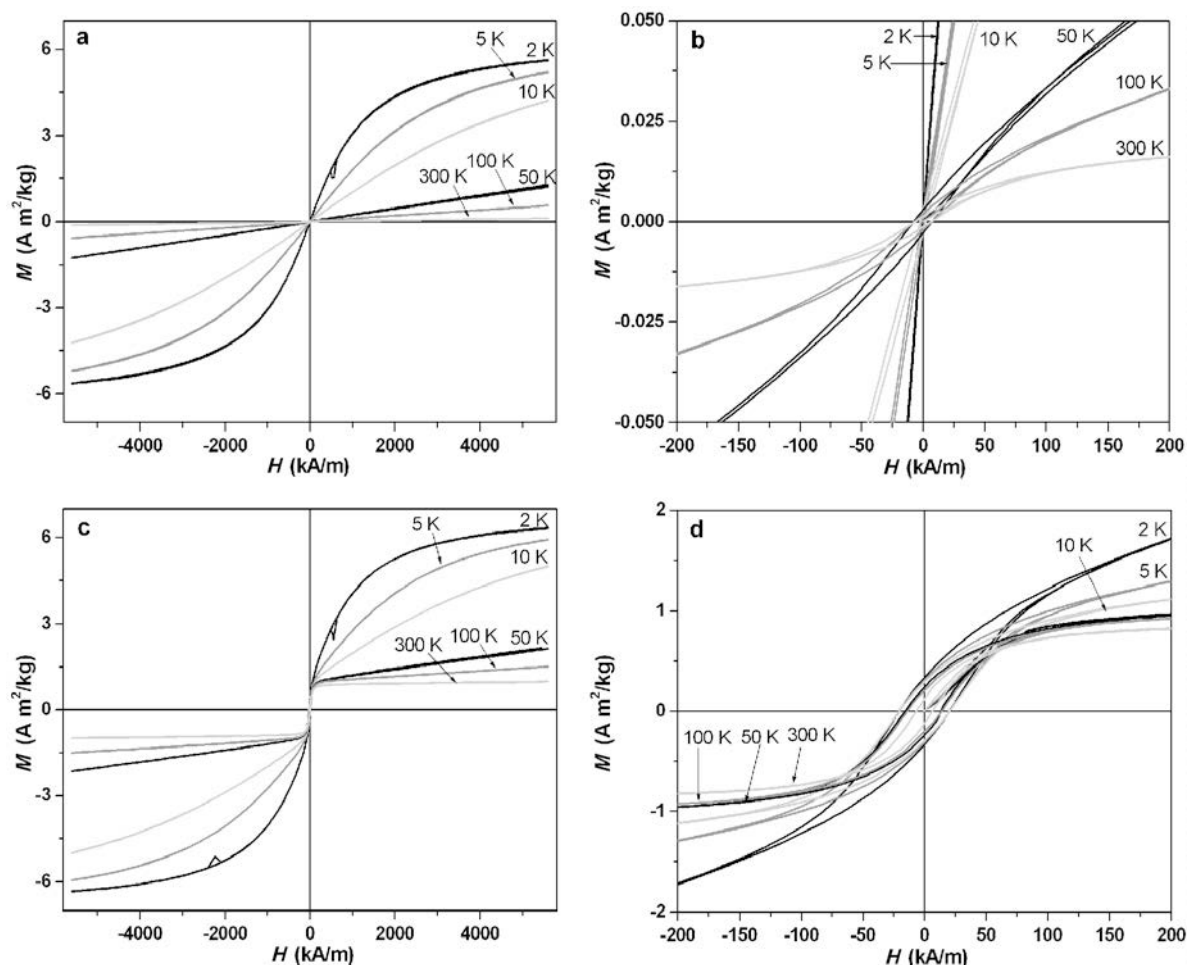


Figure 4. Hysteresis loops of Ti-M-PILC-60 (a,b) and Ti-M-PILC-500 (c,d). (a,c) full range; (b,d) close-up of loops.

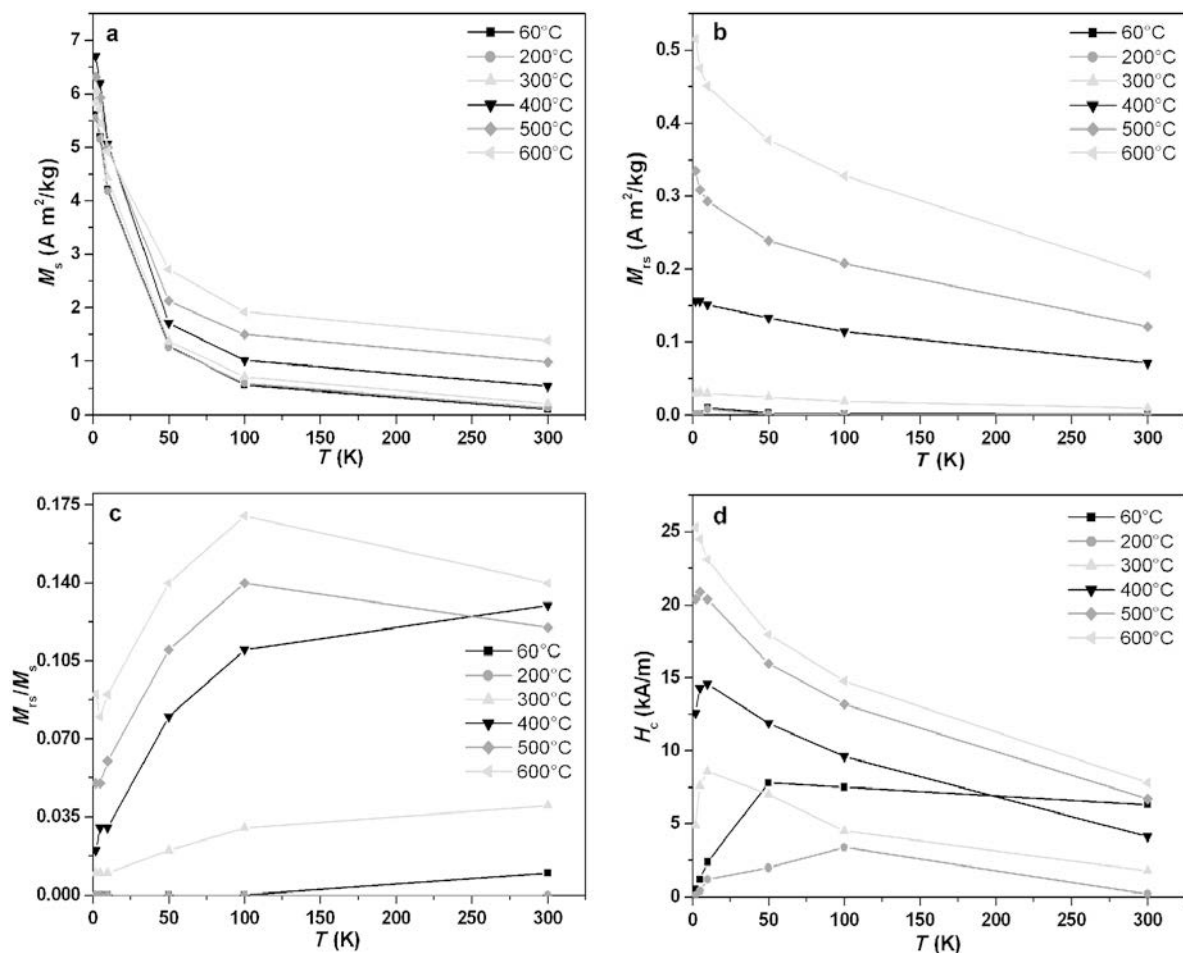


Figure 5. Temperature dependence of (a)  $M_s$ , (b)  $M_{rs}$ , (c)  $M_{rs}/M_s$ , and (d)  $H_c$  of Ti-M-PILCs as a function of measurement temperature.

are shown (Figure 5). In general, the values increase with decreasing temperature. Exceptions are Ti-M-PILC-60 and Ti-M-PILC-200.

*Saturation magnetization at room temperature.* To elucidate the nature of magnetic phases present in Ti-M-PILCs materials, as well as the magnetic order,  $M_s$  at 300 K, normalized to the additional Fe content after magnetization, were determined (Table 3). Samples Ti-M-PILC-400, -500, and -600 show the largest  $M_s$  values. Comparison with those of magnetite, maghemite, Fe metal, and  $\text{Fe}_x\text{B}$  (Moskowitz, 1991; Zhang *et al.*, 2001) suggests the presence of such phases. The presence of a poorly ordered Fe alloy must, however, also be considered.

*Magnetic-domain status.* The shape of a hysteresis loop is determined by the domain state such as single domain (SD), multi-domain (MD), pseudo-single domain (PSD), and superparamagnetism (SPM) (Muszkowicz, 1991). Loops for SD (with large  $H_c$  and  $M_{rs}$ ) materials are

typically wider than loops for MD materials. The hysteresis loop parameters  $M_{rs}/M_s$  and  $H_{cr}/H_c$  have proven very useful in distinguishing the domain state. The  $M_{rs}/M_s$ - $H_{cr}/H_c$  diagram at 300 K was compared with

Table 3. Specific saturation magnetization of Ti-M-PILCs at 300 K.

Samples	$M_s$ (A m <sup>2</sup> /kg of Fe added)
Ti-M-PILC-60	7
Ti-M-PILC-200	8
Ti-M-PILC-300	13
Ti-M-PILC-400	33
Ti-M-PILC-500	62
Ti-M-PILC-600	80
Magnetite $\text{Fe}_3\text{O}_4$	90–92
Maghemite $\gamma\text{-Fe}_2\text{O}_3$	60
Iron Fe	218
$\text{Fe}_x\text{B}$	~60

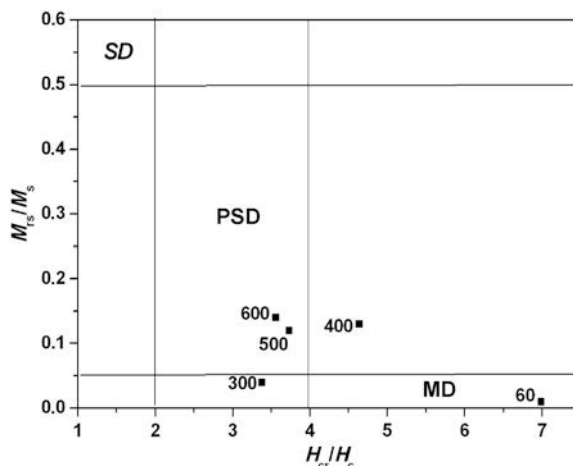


Figure 6.  $M_r/M_s$ - $H_{cr}/H_c$  diagram of Ti-M-PILCs at 300 K (domain classification after Moskowitz, 1991).

that obtained for magnetite by Muszkowicz (1991) (Figure 6). From this comparison, both Ti-M-PILC-500 and -600 exhibit a PSD state, Ti-M-PILC-300 and -400 are in the transition range between MD and PSD, Ti-M-PILC-60 might be MD. The sample Ti-M-PILC-200 lacks  $M_r$  and, therefore,  $H_{cr}$  could not be determined.

*ZFC/FC investigation.* For Ti-M-PILC-600 (similar shape to that of Ti-M-PILC-500 and -400 (Figure 7)), the curve obtained was interpreted as a broad, shallow distribution of blocking temperatures related to the presence of very weak magnetic ordering. In the case of Ti-M-PILC-60 (similar shape to those of Ti-M-PILC-200 and Ti-M-PILC-300) the plot does not show any blocking temperature.

*Determination of  $\theta$  and  $C$ .* The negative sign for  $\theta$  (Table 4) indicates that all the Ti-M-PILCs behave as

Table 4. Parameters of the Curie-Weiss-law of Ti-M-PILCs.

Samples	$\theta$ (K)	$C \times 10^6$ ( $m^3 K/kg$ )	$R^2$
Ti-M-PILC-60	-0.8	11.9	1.000
Ti-M-PILC-200	-0.7	12	1.000
Ti-M-PILC-300	-0.5	11.7	0.994
Ti-M-PILC-400	-1.9	18.1	0.962
Ti-M-PILC-500	-2.3	17.3	0.931
Ti-M-PILC-600	-4.6	23.3	0.854

ferrimagnetic materials. On the other hand, the Curie constant,  $C$ , given by:

$$C = N\mu^2/3k = N(p_{eff} \mu_B)^2/3k \quad (2)$$

increased with calcination temperature, where  $N$  is the atoms per  $cm^3$ ,  $\mu$  is the number of magnetons,  $\mu_B$  is the Bohr magneton ( $9.274,009,15(23) \times 10^{-24} J T^{-1}$ ), and  $k$  is the Boltzmann constant ( $1.3806504(24) \times 10^{-23} J K^{-1}$ ). If the number of Fe atoms,  $N$ , is estimated to be the same for all samples, the effective magnetic number of Bohr magnetons,  $p_{eff}$ , is related to  $C$  by:

$$p_{eff} = (C3k/N\mu_B^2)^{1/2} \quad (3)$$

and, therefore, increases for greater calcination temperatures. Knowing that the  $p_{eff}$  of  $Fe^{3+}$  (5.92) was greater than that of  $Fe^{2+}$  (4.90) means that the  $Fe^{3+}$  content was greater for greater calcination temperatures.

#### Mössbauer spectroscopy

Ti-M-PILCs were investigated by Mössbauer spectroscopy at room temperature. In addition to the all-ferric paramagnetic doublet which characterizes the untreated SWy-2 sample (Figure 8), a minor ferrous doublet was observed in the spectra of the samples heated at 60, 200,

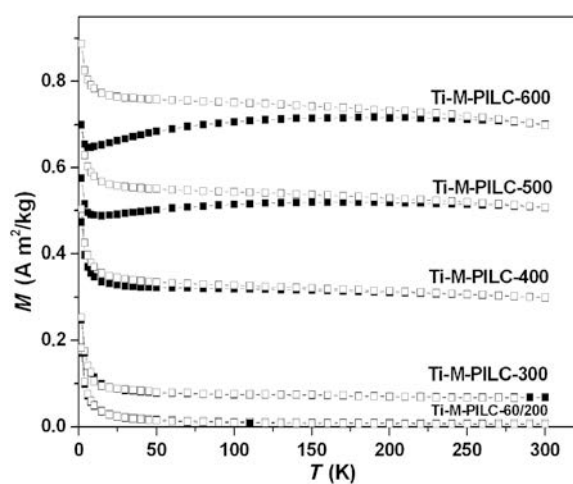


Figure 7. ZFC/FC curves of Ti-M-PILC. Filled symbols: ZFC; open symbols: FC curves.

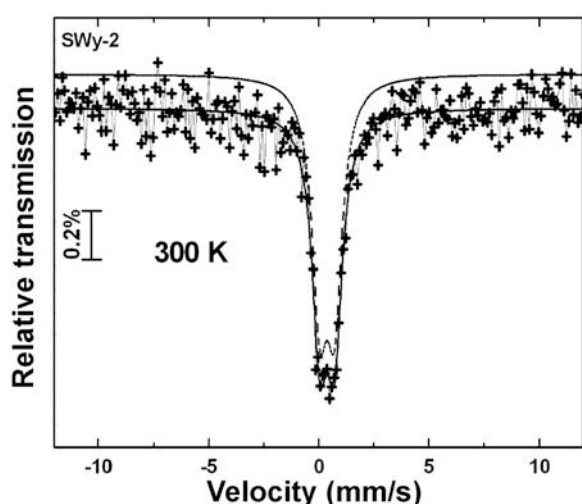


Figure 8. Mössbauer spectra of SWy-2 at room temperature.

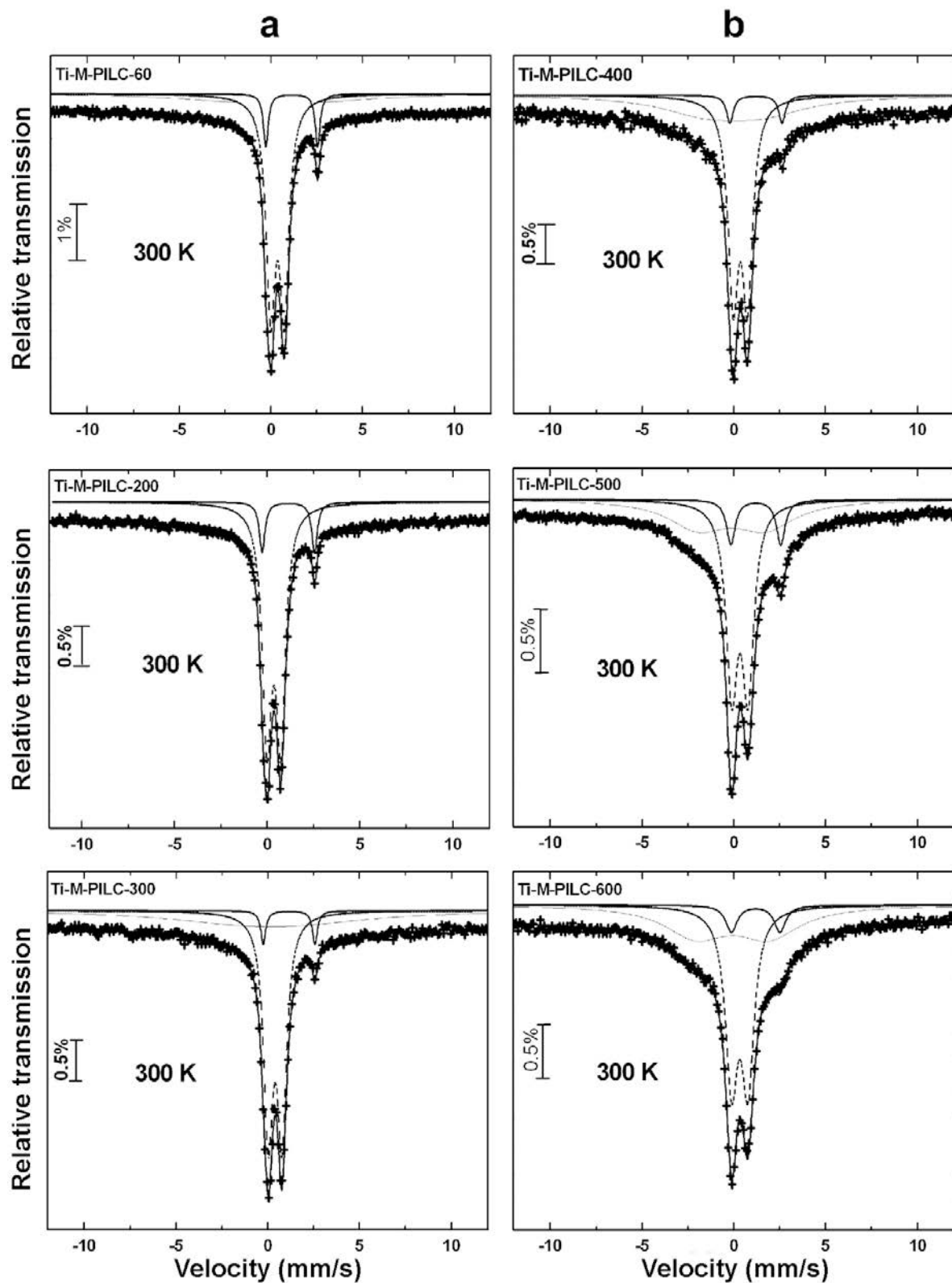


Figure 9. Mössbauer spectra of Ti-M-PILCs at room temperature.

Table 5. Fe(II):Fe(III) ratio, isomer shift (IS), and quadrupole splitting (QS) determined by Mössbauer spectroscopy of Ti-M-PILCs.

Samples	Fe <sup>2+</sup> /Fe <sup>3+</sup> ratio	Fe <sup>2+</sup> IS (mm/s)	Fe <sup>2+</sup> QS (mm/s)	Fe <sup>3+</sup> IS (mm/s)	Fe <sup>3+</sup> QS (mm/s)
Ti-M-PILC-60	0.16	1.15	2.91	0.38	0.75
Ti-M-PILC-200	0.14	1.16	2.94	0.39	0.73
Ti-M-PILC-300	0.10	1.13	2.84	0.35	0.75
Ti-M-PILC-400	0.09	1.21	2.85	0.36	0.78
Ti-M-PILC-500	0.20	1.20	2.72	0.33	0.89
Ti-M-PILC-600	0.14	1.19	2.64	0.33	0.89

and 300°C (Figure 9a), indicating that the borohydride reduction was only partially effective at reducing the ferric ions. The spectra of the samples heated at 400, 500, and 600°C exhibited, in addition to the ferric and ferrous doublets, a very broad component contributing to absorption between  $\sim\pm 4$  mm/s (Figure 9b). This broad component was interpreted as a magnetically split sextet due to FeB alloys of different compositions (Van Wonterghem *et al.*, 1986). The absence of resolved lines in the sextet was presumably caused by significant local variation in the composition (possibly including both B and Ti in the alloy). The Fe<sup>2+</sup>/Fe<sup>3+</sup> ratio (Table 5), which decreased with greater calcination temperatures up to 400°C, was in agreement with the results given by the Curie-Weiss-law calculation in the paramagnetic region. In the case of Ti-M-PILC-60, either at 300 or 3 K (Figures 9a, 10a), the Mössbauer spectra contain two distinguishable quadrupolar split resonances. A superposition of quadrupole doublets with Lorentzian line shapes was used to fit these spectra. Spectral subcomponents for Ti-M-PILC-60 have Mössbauer spectral parameters characteristic of high-spin Fe(II) and Fe(III). No magnetic ordering was observed. Similar spectra were obtained for Ti-M-PILC-200, -300, -400, -500, and -600. The spectra of Ti-M-PILC-600 at 300 and 3 K (Figures 9b, 10b) were

characterized by a distribution on relaxation times, more pronounced for 3 K. Due to this distribution, part of the sample relaxes quickly in terms of the Mössbauer time scale, giving rise to a doublet, and part of the sample relaxes slowly, giving rise to a sextet characteristic of magnetic ordering. In addition, no evidence for metallic Fe was found in any of the spectra.

## DISCUSSION

The Ti-PILC structure was affected by the reduction process. Rozenson and Heller-Kallai (1976) reported the reduction of Fe<sup>3+</sup> in octahedral positions upon treatment with hydrazine and dithionite. That reduction was reversible, as was shown using FTIR data. The band assigned to the Fe-OH-Al vibration at 870 cm<sup>-1</sup> disappeared upon reduction and reappeared following oxidation.

Reduction led to partial deterioration of the Ti-PILC-structure, following introduction of the additional Fe. This deterioration was more pronounced for the samples calcined at lower temperatures, *i.e.* for less stable samples, as indicated by the greater reduction in SSA and porosity (Table 2). The Fe in the octahedral positions was re-oxidized as the bands at 875 cm<sup>-1</sup> did not change (Figure 3b). The Mössbauer data, which

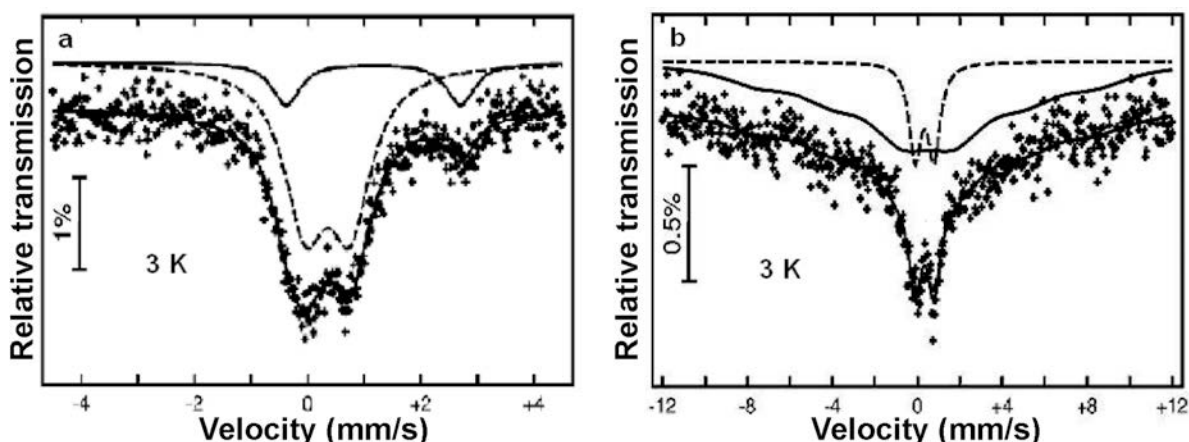


Figure 10. Mössbauer spectra at 3 K of: (a) Ti-M-PILC-60, and (b) Ti-M-PILC-600.

proved the presence of Fe(II), suggested that the divalent Fe existed solely in the phase created by the additional Fe.

The calcination temperature influenced the SSA and  $V_p$  but the Ti-PILCs reacted differently to the magnetization process, which consisted of the adsorption of Fe and reduction by NaBH<sub>4</sub>. Although the amount of additional Fe was the same for all the Ti-PILC samples, the  $M_s$  normalized to the additional amount of Fe was very different for each sample (Table 3). Some  $M_s$  values favored magnetite/maghemite phases, others favored the presence of an FeB-alloy. The Mössbauer data proved that both divalent and trivalent Fe were present, but the calculated ratios of Fe(II):Fe(III) were <0.5, the characteristic value for stoichiometric magnetite. The sign of the Weiss constant,  $\theta$ , supported the presence of a ferrimagnetic phase. Evaluation of the ratios  $M_{rs}/M_s$  and  $H_{cr}/H_c$  suggested PSD behavior, assuming magnetite particles. The behavior assumes, however, that the particle sizes are in the 50–70 nm range.

All of the arguments above suggest the presence of a poorly ordered FeB alloy. The expected particle sizes of the additional Fe-containing alloys were confined to the dimension of the interlayer space of ~1.7–1.9 nm. The Fe-alloy particles stretched wider within the interlayer, forming a thin, flat entity. The assumption of such a shape was supported by the broad and shallow FC/ZFC curves indicating a broad distribution of freezing temperatures over a large temperature range from 3 to 300 K. This prevents any long-range magnetic ordering, which was also lacking from the Mössbauer data. Only the Ti-M-PILC-600, which possessed the greatest saturation magnetization and the greatest remanence values both for magnetization and coercivity, exhibited traces of a beginning to magnetic ordering in their Mössbauer spectra at 3 K. Similar conditions, but with decreasing magnetic ordering and decreasing calcination temperature, could be assumed for the Ti-M-PILC calcined between 500 and 400°C.

Samples Ti-M-PILC-300, -200, and -60 differed in other respects from the former group of samples, although this is a rough classification. The greater relative loss in porosity and specific surface area was reflected in the temperature behavior of the magnetization (ZFC/FC) and Curie-Weiss parameters. The data, especially the Curie-constant, C, (Table 4) could be interpreted as a greater dilution of the magnetic carriers.

The greater SSA and porosity of the less-calcined samples, leading to a wider spread of the Fe particles, may thus be explained. The accessibility of the additional Fe for these less-calcined samples was promoted by the well ordered PILC layers, as indicated by the intensity of the (002) peak. For the more calcined samples, less SSA and porosity were available and the interlayer spacing was less-well pronounced, leading more easily to clustering.

The separating TOT layers hindered the formation of well ordered magnetic domains in the units, leading to the observed FC/ZFC behavior.

The presence of the two different Fe-alloy distributions, dispersed for the less calcined Ti-PILCs and clustered for the more-calcined Ti-PILCs, was due to the CEC. The less-calcined samples were more highly charged, which prevents clustering because the intercalated Fe-species must compensate the surplus negative charge.

For the samples with small CEC values, a surplus of Fe species was available, which could have adhered to the already adsorbed Fe sites within the interlayer and thus partially compensated the interlayer charge. Clustering could be promoted during the reduction process, where reduced Fe<sup>2+</sup> ions, known to be more mobile than trivalent Fe species, adsorbed to already existing clusters, similar to the process known as Ostwald ripening.

## SUMMARY AND OUTLOOK

In the present work on magnetic properties of pillared clays, the relations between porosity, CEC, and the magnetic properties upon Fe-intercalation, and subsequent reduction by NaHB<sub>4</sub> were investigated.

Large CEC values combined with large porosity and specific surface area led to an even distribution of Fe in the interlayer, causing dilution of the magnetic moments and preventing magnetic ordering.

The smaller CEC and porosity values led to clustering and the formation of magnetic units, but the presence of the TOT layers suppressed a pronounced magnetic ordering.

The data strongly suggest the presence of a poorly ordered FeB alloy. The role of the nature of the pillars is still under investigation by means of similar experiments with Al and Zr pillars.

## ACKNOWLEDGMENTS

C.B. thanks German Academic Exchange Service (DAAD) for financial support. The work of Natalie Naguib at an early stage of this work is acknowledged, as are Annett Steudel and Durime Buqezi-Ahmeti for the CEC investigations (IFG, FZK, Karlsruhe, Germany). The authors are grateful to the reviewers for their helpful corrections, comments, and suggestions.

## REFERENCES

- Booker, N.A., Keir, D., Priestley, A.J., Ritchie, C.B., Sudarmana, D.L., and Woods, M.A. (1991) Sewage clarification with magnetite particles. *Water Science and Technology*, **23**, 1703–1712.
- Brunauer, S., Emmett, P.H., and Teller, E. (1938) Adsorption of gases in multimolecular layers. *Journal of the American Chemical Society*, **60**, 309–319.
- Farmer, V.C. (1974) *The Infrared Spectra of Minerals*. Monograph 4, Mineralogical Society, London.
- Kloprogge, J.T. (1998) Synthesis of smectites and porous

- pillared clays catalysts: a review. *Journal of Porous Materials*, **5**, 5–41.
- Madejová, J. and Komadel, P. (2001) Baseline studies of the Clay Minerals Society source clays: Infrared methods. *Clays and Clay Minerals*, **49**, 410–432.
- Mak, S.Y. and Chen, D.H. (2004) Fast adsorption of methylene blue on polyacrylic acid bound iron oxide magnetic nanoparticles. *Dyes Pigments*, **61**, 93–98.
- Meier, L.P. and Kahr, G. (1999) Determination of the cation exchange capacity (CEC) of clay minerals using the complexes of copper (II) ion with triethylenetetraamine and tetraethylenepentamine. *Clays and Clay Minerals*, **47**, 386–388.
- Morrish, A.H. (1965) *The Physical Principles of Magnetism*. John Wiley & Sons, Inc., New York, London, Sydney.
- Moskowitz, B.M. (1991) *Hitchhiker's Guide to Magnetism*. The Environmental Magnetism Workshop, Institute for Rock Magnetism, University of Minnesota, USA.
- Naguib, N., Weidler, P.G., and Nüesch, R. (2003) Development of the application of magnetic micro-sorbents for the elimination of hazardous inorganic contaminants from natural waters. 10th Conference of the European Clay Groups Association, volume abstracts, p. 202.
- Neimark, A.V. and Ravikovich, P.I. (2001) Capillary condensation in MMS and pore structure characterization. *Microporous and Mesoporous Materials*, **44**, 697–707.
- Oliveira, L.C.A., Rios, R.V.R.A., Fabris, J.D., Garg, V.K., Sapag, K., and Lago, R.M. (2002) Activated carbon/iron oxide magnetic composites for the adsorption of contaminants in water. *Carbon*, **40**, 2177–2183.
- Oliveira, L.C.A., Rios, R.V.R.A., Fabris, J.D., Sapag, K., Garg, V.K., and Lago, R.M. (2003) Clay-iron oxide magnetic composites for the adsorption of contaminants in water. *Applied Clay Science*, **22**, 169–177.
- Ravikovich, P.I. and Neimark, A.V. (2001) Characterization of nanoporous materials from adsorption and desorption isotherms. *Colloids and Surfaces A: Physicochemical and Engineering Aspects*, **187**, 11–21.
- Rozenson, I. and Heller-Kallai, L. (1976) Reduction and oxidation of Fe<sup>3+</sup> in dioctahedral smectites – 1: Reduction with hydrazine and dithionite. *Clays and Clay Minerals*, **24**, 271–282.
- Sterte, J. (1986) Synthesis and properties of titanium oxide cross-linked montmorillonite. *Clays and Clay Minerals*, **34**, 658–664.
- Suzuki, M., Suzuki, I.S. and Walter, J. (2003) Quasi-two-dimensional magnetism in Ru and Rh metal layers sandwiched between grapheme sheets. *Physical Review B*, **67**, 094406.
- Thommes, M., Smarsly, B., Groene, M., Ravikovich, P.I., and Neimark, A.V. (2006) Adsorption hysteresis of nitrogen and argon in pore networks and characterization of novel micro- and mesoporous silicas. *Langmuir*, **22**, 756–764.
- Van Wonterghem, J., Morup, S., Koch, J.W., Charles, S.W., and Wells, S. (1986) Formation of ultra-fine amorphous alloy particles by reduction in aqueous solution. *Nature*, **322**, 622–623.
- Zhang, L. and Manthiram, A. (1996) Ambient temperature synthesis of fine metal particles in montmorillonite clay and their magnetic properties. *NanoStructured Materials*, **7**, 437–451.
- Zhang, Z.D., Yu, J.L., Zheng, J.G., Skorvanek, I., Kovac, J., Dong, X.L., Li, Z.J., Jin, S.R., Yang, H.C., Guo, Z.J., Liu, W., and Zhao, X.G. (2001) Structure and magnetic properties of boron-oxide-coated Fe(B) nanocapsules prepared by arc discharge in diborane. *Physical Review B*, **64**, 024404.

(Received 2 December 2008; revised 24 March 2009;  
Ms. 0247; A.E. D.C. Bain)